communications earth & environment

ARTICLE

https://doi.org/10.1038/s43247-022-00451-4 OPEN

The Eurasian epicontinental sea was an important carbon sink during the Palaeocene-Eocene thermal maximum

Mustafa Y. Kaya[1,9✉], Guillaume Dupont-Nivet[1,2,3], Joost Frieling[4,10], Chiara Fioroni[5], Alexander Rohrmann[6], Sevinç Özkan Altıner[7], Ezgi Vardar[7], Hakan Tanyaş[8], Mehmut Mamtimin[3] & Guo Zhaojie[3]

The Palaeocene-Eocene Thermal Maximum (ca. 56 million years ago) offers a primary analogue for future global warming and carbon cycle recovery. Yet, where and how massive carbon emissions were mitigated during this climate warming event remains largely unknown. Here we show that organic carbon burial in the vast epicontinental seaways that extended over Eurasia provided a major carbon sink during the Palaeocene-Eocene Thermal Maximum. We coupled new and existing stratigraphic analyses to a detailed paleogeographic framework and using spatiotemporal interpolation calculated ca. 720–1300 Gt organic carbon excess burial, focused in the eastern parts of the Eurasian epicontinental seaways. A much larger amount (2160–3900 Gt C, and when accounting for the increase in inundated shelf area 7400–10300 Gt C) could have been sequestered in similar environments globally. With the disappearance of most epicontinental seas since the Oligocene-Miocene, an effective negative carbon cycle feedback also disappeared making the modern carbon cycle critically dependent on the slower silicate weathering feedback.

[1] Institut für Geowissenschaften, Universität Potsdam, Potsdam, Germany. [2] Géosciences Rennes, CNRS – Univ. Rennes 1, Rennes, France. [3] Key Laboratory of Orogenic Belts and Crustal Evolution, Ministry of Education, Beijing, China. [4] Marine Palynology and Paleoceanography, Department of Earth Sciences, Faculty of Geosciences, Utrecht University, Utrecht, Netherlands. [5] Università degli Studi di Modena e Reggio Emilia, Dipartimento di Scienze Chimiche e Geologiche, Modena, Italy. [6] Institute of Geological Sciences, Freie Universität, Berlin, Germany. [7] Department of Geological Engineering, Middle East Technical University, Ankara, Turkey. [8] Faculty of Geo-Information Science and Earth Observation (ITC), University of Twente, Enschede, Netherlands. [9] Present address: Department of Geological Engineering, Middle East Technical University, Ankara, Turkey. [10] Present address: Department of Earth Sciences, Oxford University, Oxford, UK. ✉email: mustafayk@gmail.com

The Palaeocene-Eocene Thermal Maximum (PETM), a global warming event ca. 56 million years ago (Ma), was associated with geologically rapid release (<<10 kyr) of thousands of gigatons (Gt) of ^{13}C-depleted carbon into the ocean-atmosphere system[1–3]. The characteristic global negative Carbon Isotope Excursion (CIE) shows a rapid "onset" lasting a few kyrs, low and stable $\delta^{13}C$ values constituting the "body" of the CIE for about 70–80 kyrs, and ending by a gradual (ca. 100 kyr) "recovery"[4]. The event is marked by strongly elevated atmospheric pCO_2, substantial shoaling of the calcite compensation depth (CCD), as well as surface ocean acidification, and accelerated hydrologic cycle and weathering[5–7].

The PETM has provided broad insight into the carbon cycle, climate system, and biotic responses to environmental change that are relevant to long-term Earth climate evolution as well as future global changes[3]. However, the mechanisms responsible for the carbon release and its storage remain elusive. Distinguishing between potential processes requires assessing the timing and amount of carbon release and storage that are linked through biogeochemical feedback processes. In particular, potential carbon sinks remain to be identified and quantified in the sedimentary record[8]. Previous studies have provided evidence for carbon removal through continental weathering as evidenced by osmium (Os)[9] and lithium (Li) isotopes[10], post-event biogenic silica and carbonate (C_{carb}) accumulation in the deep ocean[11] and burial of organic carbon (C_{org}) in terrestrial and marine sediments[12,13]. Thorough analyses of sedimentary records can help constrain the timing, processes and amounts of carbon removed, and the role these processes played in the mitigation of past carbon emissions.

Importantly, organic carbon accumulation in shallow marine settings (epicontinental seas and continental shelves) has been suggested to provide a significant carbon sink for the PETM and Mesozoic Oceanic Anoxic Events (OAEs)[13–16]. We focus on the vast Eurasian Epicontinental Sea (EES) that extended from the Mediterranean Tethys to the margin of the Tibetan Plateau through the proto-Paratethys Sea and up to the Arctic through the West Siberian sea[17] (Fig. 1). Organic carbon-rich facies widely developed in the EES during the PETM[18] (Table S1). Here we estimate the amount and timing of organic carbon sequestered in the EES during the PETM using previously studied PETM records[18–25]. In addition, we generate new multi-proxy data for a recently identified section from the easternmost EES[17]. The results allow a more comprehensive view of the carbon cycle behaviour, and its implications for Cenozoic climatic events and future carbon cycle recovery.

Results

PETM record from the EES. We previously identified a Palaeocene-Eocene record from the EES (Mine section) based on biostratigraphy of dinocysts (Table S3), calcareous nannofossils (Table S4) and foraminifera (Table S5) in NW Tarim Basin, in West China[17] (Fig. 2, Fig. S1). Here, we use stable carbon isotope analyses of bulk organic matter ($\delta^{13}C_{org}$) and carbonate ($\delta^{13}C_{carb}$), to locate the characteristic PETM CIE (Fig. 2). The PETM onset is broadly expanded over ca. 2 m thickness indicating exceptionally high accumulation rates (~50 cm kyr^{-1}) given its short duration[3,26]. The overlying interval represents the CIE body ($\delta^{13}C_{org}$ values ca.−30‰) and is characterized by organic carbon-rich "sapropel" beds (Fig. 2). The onset of the recovery period is placed at ca. 11.3 m height when the bulk $\delta^{13}C_{carb}$ and $\delta^{18}O_{carb}$ values start to increase although $\delta^{13}C_{org}$ remains low (Fig. 2, see Supplementary Note 1, 2 and 4 for further geochemical and stratigraphic data presentation). The nannofossil and benthic foraminifera assemblages and reappearance of bivalves also indicate a recovery phase for this interval lacking characteristic PETM species (Samples B26, B27, Fig. 2; Fig. S3).

The expression of the PETM in the Tarim Basin is similar to most other shallow marine sections on the southern fringes of the Tethys[27] and elsewhere in the EES basin[18]. The most remarkable common feature is a dramatic increase in Total Organic Carbon (TOC) content (Fig. S2) during the sapropel deposition roughly coincident with a drop in carbonate ($CaCO_3$) content during the CIE body. Biomarker distributions, δD n-alkanes showing a drop from −143‰ to −164‰ in C_{29} and from −139‰ to −154‰ in C_{31} (Supplementary note 3; Table S2), and microfossil data across the onset signal higher siliciclastic, nutrient and fresh-water input, suggesting the drop in carbonate content is related to dilution and potentially reduced calcification (Supplementary Note 5; Fig. 2). Biomarker samples (Supplementary note 3; Table S2) also suggest a terrestrial contribution for the source of the organic matter. Similar conditions for the high-TOC sapropel beds representing the CIE body in the EES have been interpreted by previous studies using a small set of geochemical methods[22] and limited microfossil evidence showing a bloom of *Thoracosphaera* and *Braarudosphaera*[18].

The observed increase in freshwater and terrestrial input would likely have resulted in an increase in nutrient input instigating a stronger productivity and subsequently larger carbon export to the seafloor. The combination of increased export productivity and oxygen consumption during organic matter break-down ultimately led to extensive sapropel deposition. Sapropel deposition was further enhanced by the formation of a freshwater lid and sea-wide expansion of anoxic conditions[22]. Stratification due to freshwater lid in these shallow epicontinental seas allows development and persistence of oxygen-depleted waters. The terrestrial organic matter might have also partially recycled and redeposited in the EES basin enriching the TOC values[18]. Enhanced preservation of fish debris in sapropel layers suggests a shift in the reactive phosphorus (P) sink in sediments during oxygen-depleted periods, when burial of other forms of reactive P is limited[28,29]. Such conditions have been also described in other anoxic PETM EES sections (Kheu River and Guru-Fatima), where high C_{org}/P ratios indicate preferential phosphorus regeneration[22].

The extensive EES organic carbon burial appears to be concentrated in the body of the CIE. In the Mine section, the sapropel beds deposited at the base of the CIE body show the highest TOC values (max. 5%), whereas two thinner black organic-rich layers near the top of the CIE have relatively lower TOC values of ca. 1.2%.

During the recovery phase, microfossil assemblages are still dominated by low-salinity and high-nutrient taxa. Intriguingly, across this phase, there is an increase in $CaCO_3$, but not TOC, in the EES, suggesting persistent elevated carbonate precipitation in shallow seas[13] which was also observed elsewhere in deep ocean records[30].

C_{org} burial in the EES during the PETM. We estimate the amount of total organic carbon burial in the central and eastern EES based on the following equation[31].

$$M = \text{Area} * \text{Thickness} * \text{Density} * \text{TOC}. \quad (1)$$

In its simplest application, average values were used for input parameters (i.e. average thickness and TOC) for the estimation of the total amount of organic carbon burial[31]. Here, we refine this approach by including spatial variation of organic carbon burial throughout the central and eastern EES during the PETM CIE. We applied an Inverse Distance Weighted method[32] and interpolated the spatial distribution of both thickness (Fig. 3a) and TOC (Fig. 3b) based on new and previously analyzed sections

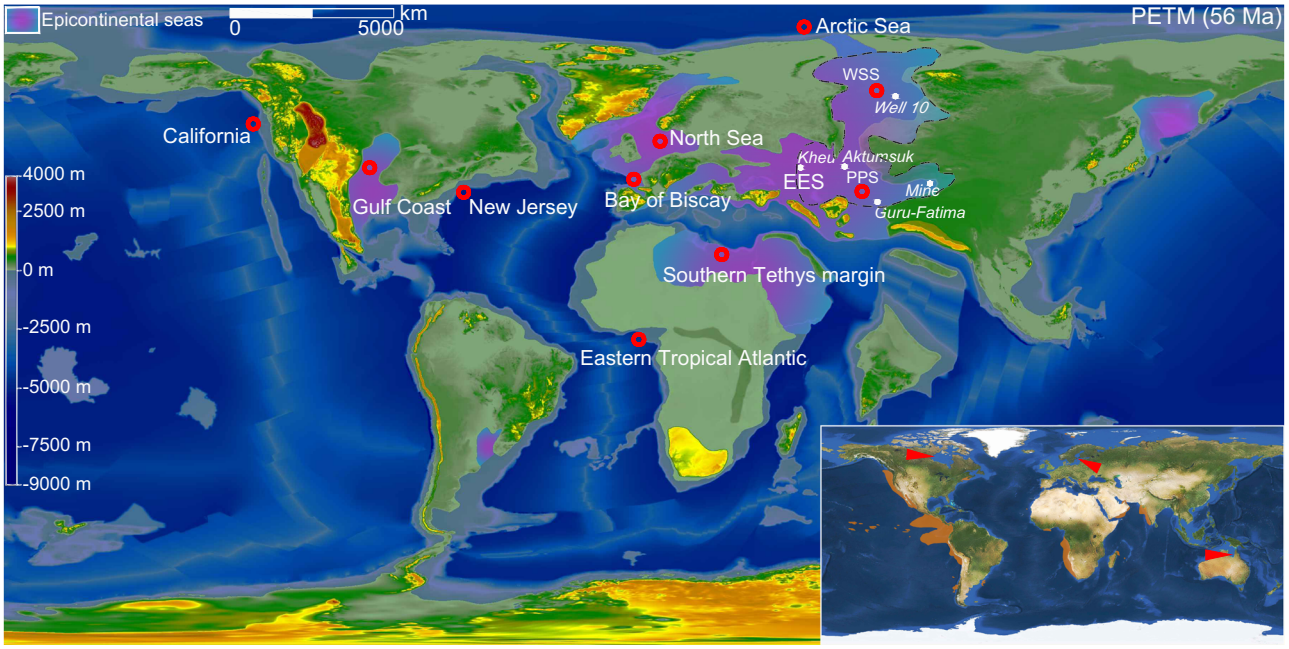

Fig. 1 Palaeogeography during the PETM (modified from ref. [34]). Until the Late Eocene isolation, the Eurasian Epicontinental Sea (EES) extended across Eurasia from the Mediterranean Tethys to the Tarim Basin in western China[17]. This study focuses on the central and eastern EES (delineated by black dashed line) consisting mostly of the West Siberian Sea (WSS) and the proto-Paratethys (PPS) that were connected via the Turgai Strait. Red circles show locations of the areas with enhanced organic carbon burial during the PETM (California and New Jersey[13]; Gulf Coast[76,77]; Bay of Biscay[80,81]; North Sea[82,83]; Eastern Tropical Atlantic[87]; Southern Tethys margin[27]; Arctic Sea[42]; see also Table 2). Black dashed line indicates the study area with enhanced organic carbon burial in EES. The inset shows the modern day epicontinental seas (red triangles; Hudson Bay, Baltic Sea and Gulf of Carpentaria) and regions with high organic carbon concentrations (ca. 1.5% or more) in marine sediments (orange shaded regions, modified from ref. [51]).

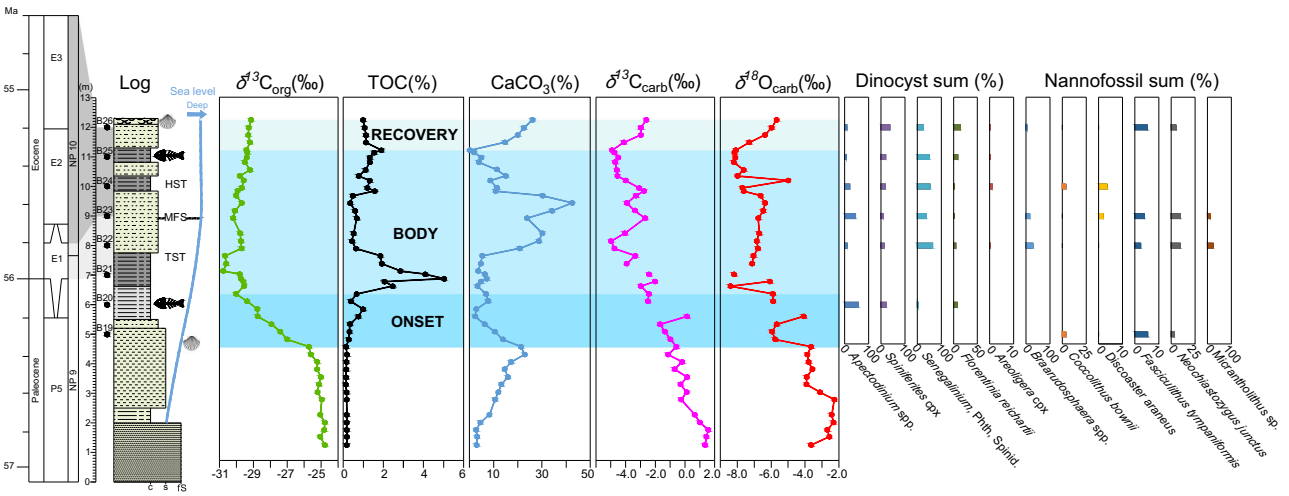

Fig. 2 The PETM record from the Mine section in the Tarim Basin. Timescale[88] indicates biostratigraphic zonations of planktonic foraminifera (P5, E1, E2 and E3) and calcareous nannofossils (NP9 and NP10). Stratigraphic log of the section shows lithologic distribution (c:clay, s:silt, fS:fine sand, sapropels in dark grey shading) with occurrences of bivalve and fish bone, biostratigraphic samples, and schematic relative sea level (blue line) interpreted from sequence stratigraphy (MFS: maximum flooding surface, TST: Transgressive systems tract, HST: Highstand systems tract). Isotopic values of $\delta^{13}C_{org}$ record the onset but not the recovery of the CIE. The recovery of the CIE starts with the increase in the bulk isotopic values of $\delta^{13}C_{carb}$ and $\delta^{18}O_{carb}$ at ca. 11.3 m height. Total Organic Carbon (TOC) values peak just after the onset and are linked to sapropel deposition. Wt%$CaCO_3$ decreases at the onset, fluctuates during CIE body, and increases at the recovery. Relative abundances (%) of dinocyst and nannofossil assemblages are indicative of paleoenvironmental conditions. The *Senegalinium* group is often interpreted to have been low-salinity tolerant, and likely had a preference for relatively high nutrients levels. *Apectodinium* and *Florentinia reichartii* are thermophilic dinocyst taxa and abundant *Spiniferites* indicate influence of open marine conditions[89]. Nannofossil *Neochiastozygus junctus* is an opportunist species indicative of high-productivity conditions[90]. *Braarudosphaera bigelowii* and *Micrantholithus* are indicative of nutrient-rich or low-salinity waters[62,91].

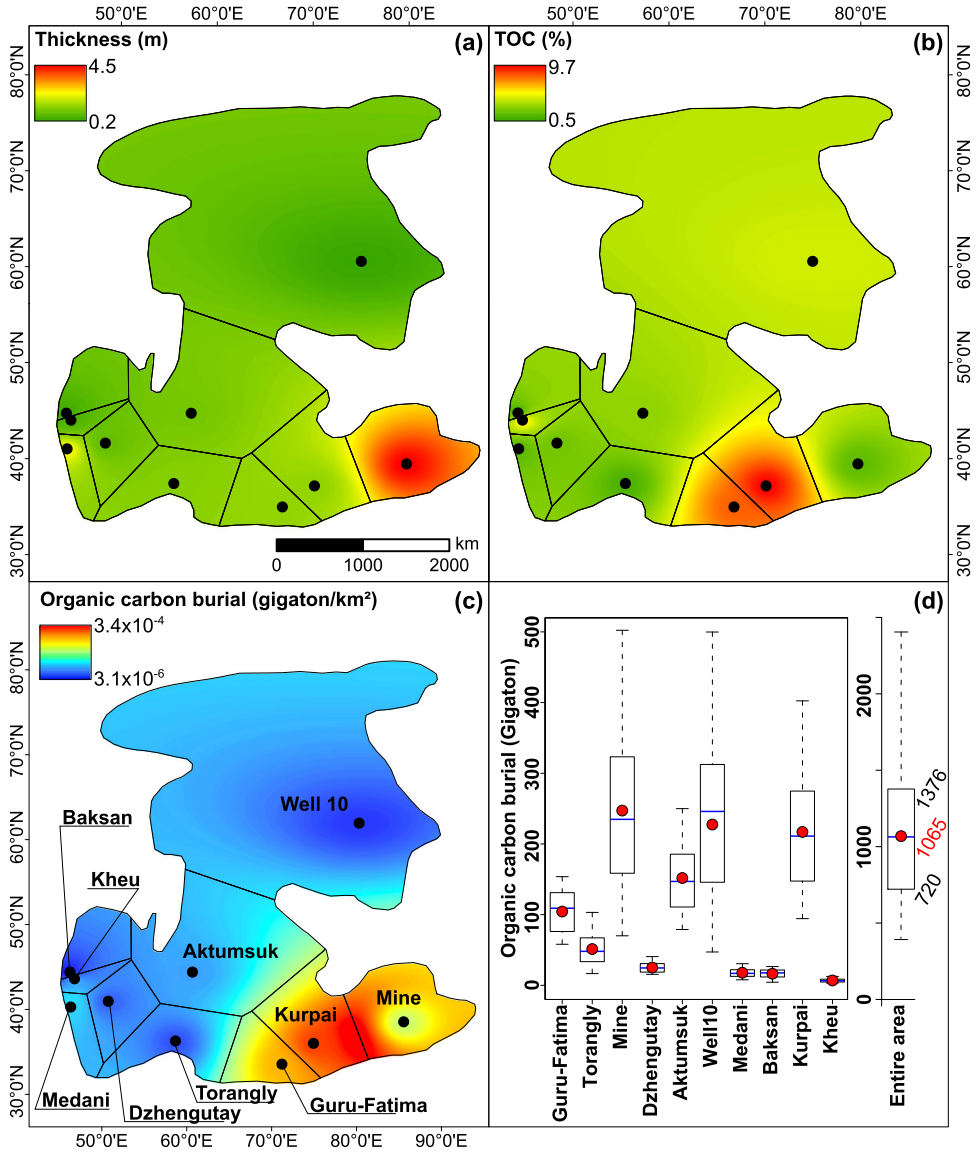

Fig. 3 Distribution of observed organic-rich sediment thickness, total organic carbon and calculated organic carbon burial in the EES. Spatial distribution of **a** organic-rich sediment thickness, **b** TOC values and **c** estimated total organic carbon burial (using 2.4×10^{12} kg km-3 density) in the proto-Paratethys and West Siberian basins during the PETM CIE. Black dots show the locations of the studied sections/wells (Mine section, this study; Well 10[25]; Kheu, Baksan, Medani, Torangly, Aktumsuk, Guru-Fatima and Kurpai sections[18,19]; Dzhengutay section[20]). Constructed Thiessen polygons indicate sub-sections with a reference section/well. **d** Box-and-whisker plots showing estimated total organic carbon burial for each sub-section and entire area. Lower and upper limits of the boxplots indicate 1st and 3rd quartiles, respectively. Red dots and blue lines inside the boxes show the mean and median values, respectively. A broad range of bulk density values (from 2.1×10^{12} to 2.7×10^{12} kg km-3) proposed for organic shales[35] was used for the estimation.

and wells (Table S1). We here use only sections and wells for which solid correlations can be made based on carbon isotope stratigraphy and that have sufficient quantitative data on sedimentary TOC content. Interpolation from these data is warranted: in the West Siberian Sea and also the wider proto-Paratethys area, there is strong supporting evidence from a much wider range of sections where biostratigraphic evidence shows coeval occurrence of organic-rich layers[33]. The organic carbon content of organic-rich successions over the PETM CIE body was estimated at each section based on integrating TOC values over their thicknesses that range from 0.2 m to 2.3 m in thickness and from 0.12 to 17% in TOC values (Table S1). All the samples used to estimate the organic carbon burial are taken exclusively from the CIE body of the PETM. The central and eastern EES extent and area (ca. 8.5×10^6 km^2; Fig. 3a, b) were determined from a review of land-sea distribution data[17] over a 60 Ma paleogeographic reconstruction[34]. We used a broad range of well-established bulk density values (from 2.1×10^{12} to 2.7×10^{12} kg km-3) proposed for organic shales[35].

We applied Eq. (1) for each grid cell (1 km × 1 km) throughout the study area using interpolated thickness and TOC with range of densities and area (i.e., area of grid cell). For a mean density value of 2.4×10^{12} kg km-3 the amount of organic carbon burial varies from 3.1×10^{-6} to 3.4×10^{-4} Gt km-2 (Fig. 3c). The cumulative amount of organic carbon burial for the entire analyzed area of the EES ranges between 891 Gt and 1147 Gt. The southeastern sector, represented by the Guru-Fatima and Kurpai sections in the Tajik Basin, and the Mine section in the Tarim Basin yields the highest organic carbon burial per km^2. The high burial in this sector may be related to the proximity of Pamir/

Tibetan Plateau orogenies, providing high siliciclastic and nutrient fluxes leading to increased productivity and sediment accumulation rates.

The substantial regional differences highlight the need for good geographical coverage and spatial interpolation techniques. To this end, the study area was divided into sub-sections (Thiessen polygons)[36] and the amount of total organic carbon burial per sub-section was examined separately. These sub-sections, the areas over which the organic carbon data from a single locality are extrapolated, were identified in such a way that all the points located inside each sub-section are closer to the associated reference point (i.e. section/well) than to any other. Firstly, the interpolated thickness and TOC values as ranges of values, which are most likely to be observed within each polygon, were obtained. We then applied Eq. (1) for each polygon accounting for variations in thickness, TOC and density. The range of total organic carbon burial for the entire area was summed for each sub-section and its associated range. This results in a total amount of organic carbon burial ranging between 720 Gt (1st quartile) and 1376 Gt (3rd quartile) with a mean value of 891 Gt in the central and eastern parts of the EES during the body of the PETM CIE (Fig. 3d).

We also used average C_{org} mass accumulation rates (C_{org} MAR; g cm-2 kyr-1, Table 1) to calculate the C_{org} burial in the EES. We first calculated mean sedimentation rates over the PETM CIE body by using the sediment thickness and an estimated CIE body duration of 75 kyr. Since we assume the same CIE body duration for the calculation of the sedimentation rates and C_{org} MAR, any variation in that estimate would not affect our result. We used a constant bulk density (g/cm^3) of 2.4. The average TOC, sediment thickness, sedimentation rates and C_{org} MAR for each polygon can be found in Table 1. The C_{org} buried for each polygon was calculated by multiplying the area and the C_{org} MAR value for that polygon. The total amount of organic carbon burial for the entire analyzed area of the EES is ca. 775 Gt which is in the range of total organic carbon burial estimated by the polygon method, indicating the estimates are robust.

For all methods, the obtained ca. 720–1300 Gt range can be almost entirely regarded as excess burial, as the pre-CIE C_{org} accumulation rate is very low with TOC values of ca. 0.1–0.2% (cumulative < 40 Gt C for the same duration).

Discussion

Epicontinental seas as C_{org} burial factories. The warm Paleogene epicontinental seas were susceptible to widespread anoxia[22] and as such provided ideal environments for the sequestration of organic carbon. In the vicinity of an orogeny, C_{org} burial appears to be further promoted by (1) weathering and/or erosion of terrestrial material supplying lithogenic sediments, nutrient influxes and terrestrial (fossil/contemporaneous) carbon and (2) increased runoff leading to stratification enhancing deoxygenation (Fig. 4a).

The shape and the bathymetry of the basin might have also influenced the variability of the C_{org} burial in (parts of) the EES. For wide, shallow epicontinental seas, the seafloor is largely flat except for the areas near shoreline. In an epicontinental sea covering an area of a foredeep and a craton, the foredeep can act as a clastic "trap" adjacent to an orogeny[37] (Fig. S4) for the coarse fraction of the delivered sediments to the epicontinental basin. In such a setting, fine-grained sediments can travel more than 100 km's from the shoreline over a largely flat epicontinental basin floor mainly by wind or tidal induced bottom current circulation[37]. Having a similar paleogeographic configuration, organic-rich mud/shale deposition might have occurred mainly on cratonward side of the EES basin to the north in shallow water depths, and less in the deep basins to the south (Fig. S4). This would be mainly due to the dilution of the fine clastics in the deep basins to the south. To the north on the craton, C_{org} burial might be variable as well depending on the distance that organic matter and the fine-grained sediments can be transported. As a result, fine clastic sedimentation and organic matter concentration would be more on the shallow proximal side of the craton (e.g., Mine, Kurpai, Guru-Fatima and Medani) with decreasing concentrations and thickness in the distal side to the North (e.g., Baksan). For localities more distal to the orogeny, redox conditions influenced by the degree of restriction, water-mass ventilation and oxygen consumption through organic matter degradation are perhaps more likely drivers of organic matter burial. The presence of persistent, low-oxygen surface and bottom waters in the eastern EES (Guru-Fatima) before and during the PETM[22] might suggest a higher degree of restriction for the eastern part of the EES leading to increased C_{org} burial.

A transgressive event at the onset of the PETM has been considered as a controlling factor on nutrient and terrestrial sediment delivery to the EES, since sea-level rise would have flooded broad shelves and coastal areas[18,19]. Despite the increasing sea level, low-salinity tolerant dinocysts and nannofossils remain persistent (Fig. 2), indicating low-salinity surface waters persisted during the PETM as also observed in the Arctic[5,38]. This suggests an exceptionally strong runoff and freshwater influx that lead to stratification.

A temporary lowered C_{org} content (ca. 1.2%) in the Mine section near the top of the CIE may indicate intermittent ventilation of bottom waters. Remarkably dinocysts and nannofossil assemblages for those intervals still indicate high nutrient levels. The continued presence of oligotrophic taxa (*Spiniferites*)

Table 1 Thickness and average TOC data for each polygon in Fig. 3.

Section/well	Thickness (m)	Avg. TOC (%)	Sedimentation rate (cm kyr-1)	C_{org} MAR (g cm-2 kyr-1)	Polygon area (10^8km^2)	C_{org} burial during the CIE body (Gt)
Kheu	0.58	6.09	0.77	0.116	0.001	8.99
Baksan	0.25	0.50	0.33	0.004	0.003	1.01
Aktumsuk-2	1.00	2.85	1.33	0.093	0.016	111.40
Torangly	1.20	1.06	1.60	0.042	0.007	21.60
Guru-Fatima	1.30	7.98	1.73	0.340	0.005	119.94
Kurpai	1.30	9.73	1.73	0.415	0.008	245.28
Medani	2.40	1.47	3.07	0.116	0.002	18.16
Well 10	0.20	4.24	0.27	0.028	0.033	67.90
Mine	4.50	1.57	6.00	0.232	0.009	164.99
Dzhengutay	0.76	2.10	1.01	0.052	0.004	16.27
TOTAL						775.53

See text for the calculation of the sedimentation rate and C_{org} MAR. The amount of C_{org} burial was calculated by multiplying the area and the C_{org} MAR value for the polygon.

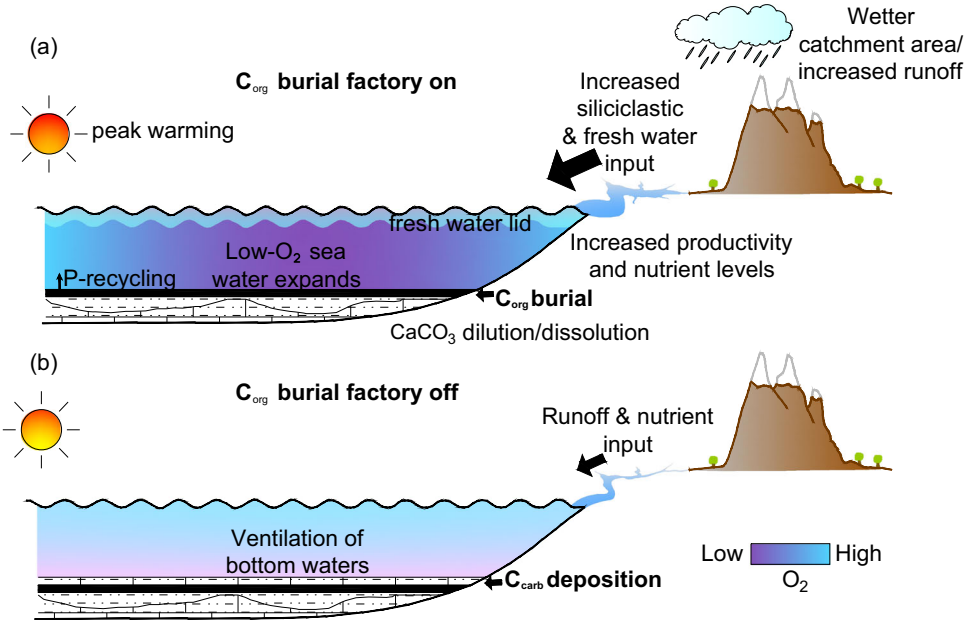

Fig. 4 Schematic representation of palaeoecological and paleoenvironmental changes in the EES during the PETM. a C_{org} burial appears to be enhanced by increased runoff leading to stratification enhancing deoxygenation and weathering and/or erosion of terrestrial material supplying lithogenic sediments, nutrient influxes and terrestrial (fossil/contemporaneous) carbon. **b** Ventilation of bottom waters shuts off the C_{org} burial factory and initiates C_{carb} deposition.

could imply transport from nearby open marine conditions to the restricted epicontinental areas. Variations in circulation may have provided occasional ventilation (Fig. 4b) in line with previously identified cyclic variations in trace metal enrichments and lycopene concentrations[22].

Combined together, we identify four main factors governing oxygenation and in turn burial efficiency of epicontinental seas; basin geometry, nutrient levels, circulation and freshwater runoff. Further positive feedbacks, including P-regeneration[22,29] are also very likely and have been argued to significantly affect the global carbon cycle[16,39].

Contribution to the global PETM carbon budget. The total global amount of carbon released during the PETM has been estimated to range from 4500 Gt[2] to more than 10,000 Gt[40] based on modelling of paleoenvironmental constraints (e.g. pH, CCD) and $\delta^{13}C$ records.

Our estimates over the central and eastern EES indicate ca. 720–1300 Gt C_{org} burial during the CIE body of the PETM. While this is perhaps 5–25% of the total released carbon, the area of the central and eastern EES (ca. 8.5×10^6 km^2) is only about 30% of the global late Palaeocene epicontinental sea surface area (ca. 30×10^6 km^2; Fig. 1). Epicontinental seaways and shelves that have been analysed also show elevated C_{org} burial across this period, warranting the extrapolation of our results (Fig. 1, Table 2). As can be seen in Table 2, highest C_{org} concentrations are mainly from the epicontinental seas and the shelves, whereas the lowest concentrations are from the bathyal/slope and outer shelf sites. There are marginal locations where enhanced C_{org} burial during the PETM is not obvious in TOC content, or offset by increased siliciclastic input such as the Svalbard (Arctic Ocean). For Svalbard sections, TOC levels are higher before the PETM (ca. 3%) and decrease (ca. 1.5%) before the onset of the PETM, and remain at this relatively lower value throughout the CIE body of the PETM[41]. However, given the relatively high TOC (ca. 1.5%) values and PETM sedimentation rates, these areas must still be considered as significant, although perhaps not enhanced, carbon sinks during the PETM[41].

On a global scale, the extrapolation of our results amounts to ca. 2160–3900 Gt excess C_{org} burial in epicontinental seas. If accurate, this implies the carbon burial in epicontinental seas alone may have sequestered 20–85% of carbon emissions. Crucially, that estimate is still without C_{org} burial in the Arctic Ocean (estimated 770 Gt C)[42] and on continental shelves.

Continental shelves were previously recognized as potentially important carbon sinks, and have been estimated to sequester 2200–2900 Gt C_{org} during the PETM[13]. However, these estimates were based on present-day shelf areas, and high Palaeocene sea level might have tripled the global shelf area[34]. We estimate a total shelf area of ca. 92×10^6 km^2 based on the paleogeographic reconstruction in Fig. 1, which when extrapolating the results of ref. [13], would impose an upper bound of the shelf C_{org} sink of ca. 7400 to 10300 Gt. Supporting our higher C_{org} burial estimate, authors of ref. [16] modelled an excess burial of ca. 13300 Gt C globally across the entire PETM in their preferred model scenario simulating C_{org} burial, satisfactorily reproducing the trends and patterns of primary productivity, deoxygenation and P recycling observed in data.

Extrapolation of our excess burial in the EES to gross global burial carries uncertainties that are inherently linked to the heterogeneous nature of the continental shelves and the epicontinental seas, as is evident from our analyses and previous studies. Clearly, the flux of organic carbon depends on a suite of local and regional factors, e.g. sedimentation rates and burial redox conditions. The uncertainty is larger in cases where there are few dedicated studies over large areas. Despite remaining uncertainty in regional and global estimates due to inherent variability, we point out that the sections where TOC content increases far outnumber the sections that show constant or declining C_{org} burial during the PETM CIE. Therefore, the basic pattern of a large increase in C_{org} burial can be observed globally. The magnitude of the C_{org} burial paired with the ubiquitous nature of increased C_{org} burial clearly shows that epicontinental seas provided a proportionally and quantitatively major C sink. Combined with epicontinental seas, continental shelves, which

Table 2 Data from the literature including average TOC during the PETM CIE, thickness of the CIE, depositional environment, C_{org} burial, deoxygenation and sediment supply for the epicontinental seas and shelves with references to the papers.

Region	Pacific		Atlantic					North Sea			Arctic Sea		Southern Tethys margin					Eastern Tropical Atlantic
	California		Gulf Coast		New Jersey		Bay of Biscay											
Section/well/location	Turney Gulch	Lodo Gulch	Harrel site	M0077 (IODP 364)	Bass River	Wilson Lake	Campo	Zumai	Fur	Grane	Store Bælt	Longyearbyen, Spitsbergen	BH9-05, Spitsbergen	(IODP) Site M0004	Gebel Nezzi, Egypt	Gebel Qreiya, Egypt	Wadi Nukhl, Egypt	Dababiya NW, Egypt	Q2-PETM,Egypt	Site 959
Average TOC during the CIE body (%)	0.16	0.16	0.40	1.93	0.58	0.37	0.92	0.22	1.64	1.35	2.84	1.49	1.60	2.80	1.5	2.7	1.55	0.82	4.43	0.83
Thickness of the CIE (m)	5	14	3	0.21	11	14	1.63	3.45	24.23	4.16	4.08	11.8	10	11	0.5*	0.4*	1.1	0.46	0.15	0.8
Depositional environment	slope	outer shelf	epc. sea	epc. sea	inner to outer shelf	inner shelf	shallow marine / transitional	bathyal	epc. sea	epc. sea	epc. sea	shelf	shelf	shelf	epc. sea	epc. sea	epc. sea	epc. sea	epc. sea	shelf
Increase in C_{org} burial	X	X	X	X	X	X	X	X	X	X	X			X	X	X	X	X	X	X
Deoxygenation			X	X	X				X	X	X	X	X	X	X	X	X	X	X	X
Increase in sediment supply	X	X		X	X	X	X	X	X	X	X	X	X	X	X	X	X	X	X	X
Reference #	13	13	76	77	13,78	13,79	80	80,81	82,83		84	41	46	42	27			85	86	87
Notes							No clear differentiation for the onset, body and recovery of the CIE					Considered as a significant carbon sink given the high PETM sedimentation rates (ca. 17 cm/kyr)			TOC (%) values are not average, they are the peak values from the CIE black shales. *thickness of the black shales, not CIE				

previously have been designated as the largest sink for C_{org}[43] (Fig. 1 inset) would have had the potential to mitigate even the high-end estimates of carbon release during the PETM. At face value, this might support modelling studies for these emission scenarios, which suggested silicate weathering alone was likely insufficient to account for the CIE recovery and force this with enhanced C_{org} burial[12,40]. However, the timing of the C_{org} burial is a critical factor. Specifically, if excess burial as modelled[16] (ca. 10,000 Gt C) and calculated in our study (7400–10300 Gt C) during the CIE body proves accurate, a broadly synchronous input of ^{13}C-depleted carbon during the body of the CIE might have to be invoked to compensate the vastly increased C_{org} burial. Such a scenario remains viable with the present data and model constraints.

Timing of C_{org} and C_{carb} burial. When looking in more detail, our estimates indicate that the bulk of the organic carbon sequestration took place during the CIE body, just after the CIE onset, whereas C_{carb} burial appears to increase somewhat later[7,30]. The exact same trends are recorded on continental shelves, where carbon sequestration also appears to occur mainly before the CIE recovery[13]. Intriguingly, a larger sink of ^{13}C-depleted C_{org}, during the CIE body requires a large and very ^{13}C-depleted carbon release, while previous studies often employ either a moderate volume (up to 5000 Gt) of extremely depleted ^{13}C input[44,45] or a large volume (>10,000 Gt) of moderately ^{13}C-depleted input[40,46] to force the CIE. The enhanced C_{org} burial hence seems to allow large fluxes of both light carbon from surface and heavy carbon from mantle reservoirs into the exogenic carbon cycle during the body phase[39].

Following this line of reasoning, the presence of sapropel layers in the EES up until the end of the CIE (Fig. 2) could suggest anomalous carbon release was active until that time and that recovery started soon after the release halted. During the recovery, disappearance of sapropel beds and the predominance of C_{carb} sedimentation indicate that C_{org} burial in the EES, also in other marginal seas, did not account for significant organic carbon sequestration. The CIE recovery should rather be ascribed to the elevated rates of C_{carb} burial due to silicate weathering feedbacks and terrestrial organic carbon storage, which involve lower organic carbon sequestration rates in line with previous estimates (from 1700 Pg C to 2900 Pg C, averaging around 2000–2500 Gt)[12,39,40].

Role of epicontinental and marginal seas from OAEs to ongoing warming. Our results highlight that during the PETM the EES and other epicontinental seas together with continental shelves provided an effective carbon sink mitigating the massive carbon injection. In particular, for the EES, this mitigation through C_{org} burial must have played a dynamic role, governed by eustatic and relative sea-level fluctuations throughout its geologic history[17,47] and its sapropel-rich sedimentary record[14].

Before the PETM, Mesozoic sedimentary successions of the EES record several intervals with C_{org}-rich deposits associated with the Jurassic and Cretaceous OAEs[14]. Most importantly, the Eocene Oligocene Transition (EOT) is coeval with the EES retreat and restriction of Paratethyan basins[48], followed by deposition of black shales with km-scale thickness and TOC values as high as 24% over vast areas from the Vienna Basin in Austria to the Caspian Sea[49]. However, the C_{org} sink provided by the epicontinental seas must have been significantly reduced after the disappearance of the Paratethys and global sea-level drop in the Oligo-Miocene[50]. This suggests other mechanisms such as C_{carb} sedimentation and silicate weathering are more efficient carbon sinks in the Late Cenozoic icehouse state.

The paucity of modern analogues with the geographic extent of the ancient epicontinental seas and reduced inundated continental shelf area as a result of much lower sea levels (Fig. 1 inset) clearly limits the potential for organic carbon burial and consequently the drawdown of atmospheric carbon dioxide. This is amplified by an anticipated decrease in global carbon burial in wetland dominated coastal systems and overall carbon preservation in the modern ocean due to anthropogenic forcing and climate change[51–53]. In addition, estimated Paleogene weatherability is comparatively low[54] and recovery from these ancient carbon cycle perturbations can be expected to considerably differ mechanistically and temporally from similar perturbations imposed on the modern carbon cycle. Specifically, the modern carbon cycle recovery may be considered critically dependent on slower negative feedbacks such as silicate weathering, perhaps until rising sea levels eventually lead to the expansion of epicontinental seas with efficient C_{org} burial factories.

Methods

Lithostratigraphy and sampling. A lithostratigraphic section was studied and measured in the NW Tarim Basin, in West China (Fig. 2, Figs. S1, and S3). The Mine section (39°50.860'N, 74°30.124'E) was chosen for excellent exposure of the Thanetian-Ypresian lower member of the Qimugen Formation and organic-rich sapropel bed unit. The lower member of the Qimugen Formation, representing the 1st Paleogene marine transgression in the Tarim Basin (Fig. S1), mainly consists of grey-to-green mudstone and marls intercalated with thin-bedded shelly limestone beds[17]. The stratigraphic thickness of the observed units was measured to a cm-level. Samples were collected with a sampling interval of 25 cm for geochemical analysis and with a sampling interval of 1 m for biostratigraphic analysis. Dinoflagellate cyst (dinocysts), calcareous nannofossils and foraminifera were used to constrain the age of the studied interval.

Biostratigraphy

Dinoflagellate cysts. Samples were processed at Palynological Laboratory Services, Holyhead, UK, using standard palynological treatment procedures. We used approximately 50 g of dry sediment for each sample. Concentrated HCl and HF were added to the sample material to remove carbonates and silicates, respectively. Organic residues were pH-neutralized and sieved over a 10 µm mesh to remove small particles. Some samples required short ultrasonic treatment or mild oxidation with HNO3. Residues were subsequently mounted on a microscope slide using glycerine jelly and analysed at 400x magnification under a light-transmitting microscope (Olympus CX41). Each slide was scanned entirely for rare species. Dinoflagellate cyst taxonomy follows ref. [55] and ref. [56] for Wetzellielloid species.

Calcareous nannofossils. Samples for calcareous nannofossils analyses were processed following the standard smear-slide techniques[57] and quantitative analyses were performed using a Zeiss Axioskop 40 microscope under crossed-polarized and plane-transmitted light at 1250x magnification, scanning at least three transverses of each slide (~600 fields of view). Nannofossil specimens were identified following the taxonomy given in refs. [58,59]. The biostratigraphic attribution is based on the scheme proposed by ref. [60] and on the recognition of secondary nannofossil bioevents[21,59,61–63].

Foraminifera. For the benthic foraminiferal taxonomy, we followed ref. [64] at generic level. Due to poor state of preservation and low abundance, identification at species level was fairly limited. Whenever possible, benthic foraminifera species were identified mainly by following the species concepts of refs. [65–68]. The taxonomy and biostratigraphic attribution of planktonic foraminifera were based on refs. [69–71].

Total Carbon (TC), Total Organic Carbon (TOC), Total Inorganic Carbon (TIC), $CaCO_3$ content and bulk organic $\delta^{13}C_{org}$ analyses. For the TC determination, ca. 3 mg of sample material was loaded in tin capsules (5 × 9 mm) and finally wrapped and measured.

The TOC content and $\delta^{13}C_{org}$ values were determined on in-situ decalcified samples. Around 6 mg of sample material was weighted into 5 × 9 mm Ag-capsules, dropped with 20% HCl, heated for 3 h at 75 °C, and finally wrapped and measured.

Analyses of elemental content and isotopic composition were performed using an elemental analyser (EA) (NC2500 CarloErba) coupled with a ConFlo III interface on a DELTAplusXL isotopic ratio mass spectrometer (IRMS) (ThermoFischer Scientific) at the GeoForschungsZentrum in Potsdam, Germany.

The isotopic composition is given in standard delta notation: $\delta(‰) = [(R_{sample} - R_{standard})/R_{standard}] \times 1000$. The ratio ($R$) and standard for carbon is $^{13}C/^{12}C$ and VPDB (Vienna PeeDee Belemnite). The TC and TOC contents were calibrated using Urea and the results were verified with a soil reference sample (Boden3, Hekatech). The calibration for isotopic ratios was performed using certified isotope standards (USGS24, IAEA CH-7), and verified with Pepton and a soil reference sample (Boden3, Hekatech). The reproducibility for replicate analyses is 0.2% for carbon content and 0.15 ‰ for $\delta^{13}C_{org}$, respectively.

The TIC content was calculated using the difference between TC and TOC. With the TIC content we calculated the $CaCO_3$ content using the factor 8.33.

Bulk carbonate $\delta^{13}C_{carb}$ & $\delta^{18}O_{carb}$ analyses. Bulk sedimentary carbonate isotope analyses were performed at Utrecht University following standard procedures. Briefly, ca. 0.5 g of freeze-dried sediments were homogenized and a sedimentary weight yielding approximately 100 µg of pure carbonate was analysed. CO_2 was generated from the carbonate by adding phosphoric acid (H_3PO_4) at 70 °C using continuous flow GC-IRMS. Both internal (Naxos) and external (IAEA-CO-1) carbonate standards were run along samples to obtain absolute stable carbon and oxygen isotope values. Reproducibility of the $\delta^{13}C_{carb}$ and $\delta^{18}O_{carb}$ were in the order of 0.1‰ or better, except for samples with very low carbonate content. $\delta^{13}C_{carb}$ and $\delta^{18}O_{carb}$ values are reported relative to the VPDB standard.

Biomarker analysis. Samples were crushed using dichloromethane (DCM)-cleaned equipment and pulverized (ca. 40–60 µm) in a shatterbox with agate grinding chamber. Soluble organic matter was extracted from samples (ca. 100 g) at the GFZ Potsdam using an accelerated solvent extractor (ASE350, Dionex Crop., Sunnyvale, USA) with a dichloromethane/methanol mixture of 9:1 at 100 °C and 1500 psi. Total extracts of three 18-min cycles were captured in 250 ml bottles, concentrated to 4 ml in a Turbovap, and then separated on silica gel using a solid phase extraction (SPE). SPE-columns preparation included the use of 1.5 g of silica gel (0.040–0.063 mesh; Alfa Aesar, Ward Hill, USA) filled into 6 ml glass columns (Macherey-Nagel, Düren, Germany). Columns were cleaned with three times the column volume of acetone and DCM and then dried overnight at 60 °C. The column was again flushed with three times the column volume of acetone, DCM, and hexane prior to transferal of the total lipid extract onto the column. n-Alkanes and alcohols were eluted in 15 ml hexane and DCM, respectively, and the remaining substances were flushed with 15 ml methanol. Two out of three separated fractions were stored for later analysis. The remaining n-alkane fraction was treated with 6 µg 5-androstane standard for gas chromatographic quantification. The identification and quantification of individual compounds was performed using a gas chromatograph with a coupled flame ionization and mass-selective detector (GC-FID/MSD Agilent 7890 A GC, 5975 C MSD, Agilent Technologies, Palo Alto, USA) flushed with helium carrier gas. Temperatures in the GC oven were programmed to increase at a rate of 12 °C/min starting from 70 °C to 320 °C at which temperatures were held constant for 21 min. The PTV injector had a split ratio of 5:1 at an initial temperature of 70 °C. The injector was heated up to 300 °C at a programmed rate of 7.2 °C/min and held constant at this temperature for 2.5 min. The n-alkane FID-peak areas were compared with the previously added 5-androstane standard from which n-alkane concentrations were calculated. For all samples, δ13Cwax were measured using a coupled gas chromatography-isotope ratio mass spectrometer (GC-IRMS) Delta V Advantage (ThermoFisher Bremen, Germany) at the University of Connecticut. The n-alkane fractions were concentrated to 60 µg/µl in hexane for $\delta^{13}C$ measurements. The n-alkane fraction was injected (1 µl) into an TRACE 1310 Gas Chromatograph equipped with an Agilent DB-5 column, 30 m × 0.25 mm × 25 µm film. The injector was operated in splitless mode at 300 °C and the oven was held at 70 °C for 2 min. The oven was heated at 15 °C/min until 150 °C, and then heated with 5 °C/min to 320 °C. The final temperature was held for 10 min. The column effluent was transferred via a ConFlo IV interface (ThermoFisher, Bremen, Germany) into an isotope ratio mass spectrometer after conversion to H_2 in a high-temperature oven at 960 °C. Duplicates were measured for each sample and a CO2 gas with known isotopic composition was used as reference gas. The same n-alkane standard mixtures (A3-5 and B2 standard) were used as for δD measurements with the same standard setup in the measured sequence. Only duplicate analysis for each sample was performed. The standards were used to correct the analysed samples to Vienna Standard Pee Dee Belemnite scale (VPDB). A Linear regression was produced using the known vs. measured values of the A4 and A5 standards and linear regression had a slope of 1 ± 0.14 for all analysed standards. The results are reported in delta notation in permil (‰). The analytical precision of each single measurement had a typical standard deviation of ±0.5‰. We report all measured samples with a standard deviation of ±1‰, which represents the total variability in all measured n-alkane standard mixtures of the A3-5 standards and is more than the analytical standard deviation of ±0.5‰.

Relative sea level. Sedimentary facies and micropaleontologic assemblages have been used to reconstruct water depths and recognize sea-level rise (or fall) generally expressed by a shift to offshore (or inshore) characteristics[72]. The distribution and relative abundance of planktonic and benthic foraminifera have been used to further identify relative sea level variations[73,74]. Relative abundance of terrestrially derived palynomorphs and other organic material, along with grain size of the deposited sediments, were inspected to assess coastal proximity[75].

Data availability

All relevant data are included in the manuscript and Supplementary Information files. Supplementary data 1, the minimum dataset required to reproduce the findings, can also be found from https://figshare.com/articles/dataset/Supplementary_data_1/19609722.

Received: 24 November 2021; Accepted: 9 May 2022;
Published online: 31 May 2022

References

1. Dickens, G. R., O'Neil, J. R., Rea, D. K. & Owen, R. M. Dissociation of oceanic methane hydrate as a cause of the carbon isotope excursion at the end of the Paleocene. *Paleoceanography* **10**, 965–971 (1995).
2. Zeebe, R. E., Zachos, J. C. & Dickens, G. R. Carbon dioxide forcing alone insufficient to explain Palaeocene–Eocene Thermal Maximum warming. *Nat. Geosci.* **2**, 576 (2009).
3. Zeebe, R. E., Ridgwell, A. & Zachos, J. C. Anthropogenic carbon release rate unprecedented during the past 66 million years. *Nat. Geosci.* **9**, 325 (2016).
4. McInerney, F. A. & Wing, S. L. The Paleocene-Eocene Thermal Maximum: a perturbation of carbon cycle, climate, and biosphere with implications for the future. *Annual Rev. Earth Planet. Sci.* **39**, 489–516 (2011).
5. Pagani, M. et al. Arctic hydrology during global warming at the Palaeocene/Eocene thermal maximum. *Nature* **442**, 671 (2006).
6. Penman, D. E., Hönisch, B., Zeebe, R. E., Thomas, E. & Zachos, J. C. Rapid and sustained surface ocean acidification during the Paleocene-Eocene Thermal Maximum. *Paleoceanography* **29**, 357–369 (2014).
7. Zachos, J. C. et al. Rapid acidification of the ocean during the Paleocene-Eocene Thermal Maximum. *Science* **308**, 1611–1615 (2005).
8. Junium, C. K., Dickson, A. J. & Uveges, B. T. Perturbation to the nitrogen cycle during rapid Early Eocene global warming. *Nat. Commun.* **9**, 1–8 (2018).
9. Ravizza, G., Norris, R. N., Blusztajn, J. & Aubry, M. P. An osmium isotope excursion associated with the late Paleocene thermal maximum: evidence of intensified chemical weathering. *Paleoceanography* **16**, 155–163 (2001).
10. Pogge von Strandmann, P. A. et al. Lithium isotope evidence for enhanced weathering and erosion during the Paleocene-Eocene Thermal Maximum. *Sci. Adv.* **7**, eabh4224 (2021).
11. Penman, D. E. Silicate weathering and North Atlantic silica burial during the Paleocene-Eocene Thermal Maximum. *Geology* **44**, 731–734 (2016).
12. Bowen, G. J. & Zachos, J. C. Rapid carbon sequestration at the termination of the Palaeocene–Eocene Thermal maximum. *Nat. Geosci.* **3**, 866 (2010).
13. John, C. M. et al. North American continental margin records of the Paleocene-Eocene thermal maximum: implications for global carbon and hydrological cycling. *Paleoceanography* https://doi.org/10.1029/2007PA001465 (2008).
14. Gavrilov, Y. O., Shcherbinina, E. A. & Aleksandrova, G. N. Mesozoic and early Cenozoic Paleoecological events in the sedimentary record of the NE Peri-Tethys and adjacent areas: an overview. *Lithol. Miner. Res.* **54**, 524–543 (2019).
15. Jenkyns, H. C. Geochemistry of oceanic anoxic events. *Geochem. Geophys. Geosys.* https://doi.org/10.1029/2009GC002788 (2010).
16. Papadomanolaki, N. M., Sluijs, A. & Slomp, C. P. Eutrophication and deoxygenation forcing of marginal marine organic carbon burial during the PETM. *Paleoceanogr. Paleoclimatol.* https://doi.org/10.1029/2021PA004232 (2022).
17. Kaya, M. Y. et al. Paleogene evolution and demise of the proto-Paratethys Sea in Central Asia (Tarim and Tajik basins): role of intensified tectonic activity at ca. 41 Ma. *Basin Res.* **31**, 461–486 (2019).
18. Gavrilov, Y. O., Shcherbinina, E. A. & Oberhänsli, H. In *Causes and Consequences of Globally Warm Climates in the Early Paleogene* Vol. 369 (eds Wing, S.L. et al.) 147–168. (Geological Society of America, 2003).
19. Gavrilov, Y. O., Kodina, L. A., Lubchenko, I. Y. & Muzylev, N. G. The late Paleocene anoxic event in epicontinental seas of Peri-Tethys and formation of the sapropelite unit: sedimentology and geochemistry. *Lithol. Miner.Resour.* **32**, 427–450 (1997).
20. Gavrilov, Y. O., Shcherbinina, E. A., Golovanova, O. & Pokrovsky, B. *Climatic and Biotic Events of the Paleogene [CBEP 2009], Extended Abstracts From an International Conference in Wellington* Vol. 18 (GNS Science Miscellaneous Series, New Zealand, 2009).
21. Shcherbinina, E. et al. Environmental dynamics during the Paleocene–Eocene thermal maximum (PETM) in the northeastern Peri-Tethys revealed by high-resolution micropalaeontological and geochemical studies of a Caucasian key section. *Palaeogeogr. Palaeoclim. Palaeoecol.* **456**, 60–81 (2016).
22. Dickson, A. J. et al. The spread of marine anoxia on the northern Tethys margin during the Paleocene-Eocene Thermal Maximum. *Paleoceanography* **29**, 471–488 (2014).
23. Dickson, A. J. et al. Evidence for weathering and volcanism during the PETM from Arctic Ocean and Peri-Tethys osmium isotope records. *Palaeogeogr. Palaeoclimatol. Palaeoecol.* **438**, 300–307 (2015).
24. Bolle, M. P. et al. The Paleocene–Eocene transition in the marginal northeastern Tethys (Kazakhstan and Uzbekistan). *Int. J. Earth Sci.* **89**, 390–414 (2000).
25. Frieling, J. et al. Paleocene-Eocene warming and biotic response in the epicontinental West Siberian Sea. *Geology* **42**, 767–770 (2014).
26. Kirtland Turner, S., Hull, P. M., Kump, L. R. & Ridgwell, A. A probabilistic assessment of the rapidity of PETM onset. *Nat. Commun.* **8**, 1–10 (2017).
27. Speijer, R. & Wagner, T. Sea-level changes and black shales associated with the late Paleocene thermal maximum: organic-geochemical and micropaleontologic evidence from the southern Tethyan margin (Egypt-Israel). *Catastrophic Events and Mass Extinctions* **356**, 533–549. (2002).
28. Slomp, C. P. & Van Cappellen, P. The global marine phosphorus cycle: sensitivity to oceanic circulation. *Biogeosci. Discuss.* **3**, 1587–1629 (2006).
29. Tsandev, I. & Slomp, C. P. Modeling phosphorus cycling and carbon burial during Cretaceous Oceanic Anoxic Events. *Earth Planet. Sci. Lett.* **286**, 71–79 (2009).
30. Penman, D. E. et al. An abyssal carbonate compensation depth overshoot in the aftermath of the Palaeocene–Eocene Thermal Maximum. *Nat. Geosci.* **9**, 575–580 (2016b).
31. Xu, W. et al. Carbon sequestration in an expanded lake system during the Toarcian oceanic anoxic event. *Nat. Geosci.* **10**, 129 (2017).
32. Watson, D. F. & Philip, G. M. A refinement of inverse distance weighted interpolation. *Geoprocessing* **2**, 315–327 (1985).
33. Radionova, E. P. et al. Early Paleogene transgressions: stratigraphical and sedimentological evidence from the northern Peri-Tethys. *Geol. Soc. Am. Spec. Pap.* **369**, 239–262 (2003).
34. Poblete, F. et al. Towards interactive global paleogeographic maps, new reconstructions at 60, 40 and 20 Ma. *Earth Sci. Rev.* **214**, 103508 (2021).
35. Vernik, L. & Milovac, J. Rock physics of organic shales. *The Leading Edge* **30**, 318–323 (2011).
36. Thiessen, A. H. Precipitation averages for large areas. *Mon. Weather Rev.* **39**, 1082–1089 (1911).
37. Schieber, J. Mud re-distribution in epicontinental basins–Exploring likely processes. *Marine and Petroleum Geol.* **71**, 119–133 (2016).
38. Sluijs, A. et al. Subtropical Arctic Ocean temperatures during the Palaeocene/Eocene thermal maximum. *Nature* **441**, 610–613 (2006).
39. Komar, N. & Zeebe, R. E. Redox-controlled carbon and phosphorus burial: a mechanism for enhanced organic carbon sequestration during the PETM. *Earth and Planetary Sci. Lett.* **479**, 71–82 (2017).
40. Gutjahr, M. et al. Very large release of mostly volcanic carbon during the Palaeocene–Eocene Thermal Maximum. *Nature* **548**, 573 (2017).
41. Harding, I. C. et al. Sea-level and salinity fluctuations during the Paleocene–Eocene thermal maximum in Arctic Spitsbergen. *Earth Planet. Sci. Lett.* **303**, 97–107 (2011).
42. Sluijs, A. et al. Arctic late Paleocene–early Eocene paleoenvironments with special emphasis on the Paleocene-Eocene thermal maximum (Lomonosov Ridge, Integrated Ocean Drilling Program Expedition 302). *Paleoceanography* https://doi.org/10.1029/2007PA001495 (2008).
43. Blair, N. E., Leithold, E. L. & Aller, R. C. From bedrock to burial: the evolution of particulate organic carbon across coupled watershed-continental margin systems. *Marine Chemistry* **92**, 141–156 (2004).
44. Dickens, G. R., Castillo, M. M. & Walker, J. C. A blast of gas in the latest Paleocene: simulating first-order effects of massive dissociation of oceanic methane hydrate. *Geology* **25**, 259–262 (1997).
45. Frieling, J. et al. Thermogenic methane release as a cause for the long duration of the PETM. *Proc. Nat. Acad.f Sci.* **113**, 12059–12064 (2016).
46. Cui, Y. et al. Slow release of fossil carbon during the Palaeocene–Eocene Thermal Maximum. *Nat. Geosci.* **4**, 481–485 (2011).
47. Kaya, M. Y. et al. Cretaceous evolution of the Central Asian Proto-Paratethys sea: Tectonic, Eustatic, and climatic controls. *Tectonics* **39**, e2019TC005983 (2020).
48. Schulz, H. M., Bechtel, A. & Sachsenhofer, R. F. The birth of the Paratethys during the Early Oligocene: from Tethys to an ancient Black Sea analogue? *Glob. Planet. Change* **49**, 163–176 (2005).
49. Sachsenhofer, R. F. et al. Paratethyan petroleum source rocks: an overview. *J. Pet. Geol.* **41**, 219–245 (2018).
50. Sant, K., Palcu, D. V., Mandic, O. & Krijgsman, W. Changing seas in the Early–Middle Miocene of Central Europe: a Mediterranean approach to Paratethyan stratigraphy. *Terra Nova* **29**, 273–281 (2017).
51. Keil, R. Anthropogenic forcing of carbonate and organic carbon preservation in marine sediments. *Annu. Rev. Mar. Sci.* **9**, 151–172 (2017).
52. Hopkinson, C. S., Cai, W. J. & Hu, X. Carbon sequestration in wetland dominated coastal systems—a global sink of rapidly diminishing magnitude. *Curr. Opin. Environ. Sustain.* **4**, 186–194 (2012).
53. Syvitski, J. P., Vörösmarty, C. J., Kettner, A. J. & Green, P. Impact of humans on the flux of terrestrial sediment to the global coastal ocean. *Science* **308**, 376–380 (2005).
54. Caves, J. K., Jost, A. B., Lau, K. V. & Maher, K. Cenozoic carbon cycle imbalances and a variable weathering feedback. *Earth Planet Sci. Lett.* **450**, 152–163 (2016).
55. Williams, G.L., Fensome, R.A. and MacRae, R.A. The Lentin and Williams index of fossil dinoflagellates 2017 edition. Vol. 48 (American Association of Stratigraphic Palynologists Foundation, 2017).

56. Bijl, P. K. et al. Comment on "Wetzeliella and its allies—the 'hole' story: a taxonomic revision of the Paleogene dinoflagellate subfamily Wetzelielloideae" by Williams et al. (2015). *Palynology* **6122**, 1–7 (2016).
57. Bown, P. R. & Young, J. R. *Calcareous Nannofossil Biostratigraphy* (Chapman & Hall, London, 1998)
58. Perch-Nielsen, K. *Plankton Stratigraphy* (Cambridge University Press, Cambridge, 1985).
59. Agnini, C. et al. Biozonation and biochronology of Paleogene calcareous nannofossils from low and middle latitudes. *Newsl. Stratigr.* https://doi.org/10.1127/0078-0421/2014/0042 (2014).
60. Martini, E. Standard Tertiary and Quaternary calcareous nannoplankton zonation. In *Proc. 2nd International Conference Planktonic Microfossils Roma*: Rome (ed. Tecnosci.) 739–785 (Tecnoscienza, Roma, 1971).
61. Bralower, T. J. Evidence of surface water oligotrophy during the Paleocene–Eocene thermal maximum: nannofossil assemblage data from Ocean Drilling Program Site 690, Maud Rise, Weddell Sea. *Paleoceanography* **17**, 1–11 (2002).
62. Bown, P. R. Paleogene calcareous nannofossils from the Kilwa and Lindi areas of coastal Tanzania: Tanzania Drilling Project Sites 1 to 10. *J. Nannoplankton Res.* **27**, 21–95 (2005).
63. Raffi, I., Backman, J. & Pälike, H. Changes in calcareous nannofossil assemblages across the Paleocene/Eocene transition from the paleo-equatorial Pacific Ocean. *Palaeogeogr. Palaeoclimatol. Palaeoecol.* **226**, 93–126 (2005).
64. Loeblich, AR.J. and Tappan, H. *Foraminiferal Genera and Their Classification*. (Van Nostrand Reinhold, NY, 1988).
65. Cushman, J. A. Paleocene foraminifera of the Gulf coastal region of the United States and adjacent areas. *U.S. Geol. Surv. Prof. Pap.* **232**, 75 (1951).
66. LeRoy, L. W. Biostratigraphy of the Maqfi section, Egypt. *GSA Mem* **54**, 73 (1953).
67. Berggren, W. A. & Aubert, J. Paleocene benthonic foraminiferal biostratigraphy, paleobiogeography and paleoecology of Atlantic-Tethyan regions: Midway-type fauna. *Palaeogeogr. Palaeoclimatol. Palaeoecol.* **18**, 73–192 (1975).
68. Speijer, R. P. Extinction and recovery patterns in benthic foraminiferal paleocommunities across the Cretaceous/Paleogene and Paleocene/Eocene boundaries. *Geol. Ultraiectina* **124**, 191 (1994).
69. Olsson, R. K., Hemleben, C., Berggren, W. A. & Huber, B. T. (eds) *Atlas of Paleocene Planktonic Foraminifera, Smithsonian Contributions to Paleobiology* (Cushman Foundation, 1999).
70. Pearson, P. N., Olsson, R. K., Huber, B. T., Hemleben, C. & Berggren, W. A. (eds) *The Atlas of Eocene Planktonic Foraminifera, Cushman Foundation Special Publication* (Cushman Foundation, 2006).
71. Young, J. R., Wade, B. S. & Huber B. T. *pforams@mikrotax website*. http://www.mikrotax.org/pforams (2018).
72. Catuneanu, O. *Principles of Sequence Stratigraphy* (Elsevier, 2006).
73. BouDagher-Fadel, M. K. *Biostratigraphic and Geological Significance of Planktonic Foraminifera* Vol. 22 (UCL Press, 2012).
74. Murray, J. W. *Ecology and Applications of Benthic Foraminifera* (Cambridge University Press, 2006).
75. Sluijs, A. et al. Eustatic variations during the Paleocene-Eocene greenhouse world. *Paleoceanography* https://doi.org/10.1029/2008PA001615 (2008).
76. Sluijs, A. et al. Warming, euxinia and sea level rise during the Paleocene–Eocene Thermal Maximum on the Gulf Coastal Plain: implications for ocean oxygenation and nutrient cycling. *Clim. Past* **10**, 1421–1439 (2014).
77. Smith, V. et al. Life and death in the Chicxulub impact crater: a record of the Paleocene–Eocene Thermal Maximum. *Clim. Past* **16**, 1889–1899 (2020).
78. Stassen, P., Thomas, E. & Speijer, R. The progression of environmental changes during the onset of the Paleocene-Eocene Thermal Maximum (New Jersey Coastal Plain). *Austrian J. Earth Sci.* **105**, 169–178 (2012).
79. Zachos, J. C. et al. Extreme warming of mid-latitude coastal ocean during the Paleocene-Eocene Thermal Maximum: inferences from TEX86 and isotope data. *Geology* ***34***, 737–740 (2006).
80. Manners, H. R. et al. Magnitude and profile of organic carbon isotope records from the Paleocene–Eocene Thermal Maximum: evidence from northern Spain. *Earth Planet. Sci. Lett.* **376**, 220–230 (2013).
81. Dunkley Jones, T. et al. Dynamics of sediment flux to a bathyal continental margin section through the Paleocene–Eocene Thermal Maximum. *Clim. Past* **14**, 1035–1049 (2018).
82. Jones, M. T. et al. Mercury anomalies across the Palaeocene–Eocene Thermal Maximum. *Clim. Past* **15**, 217–236 (2019).
83. Stokke, E. W. et al. Rapid and sustained environmental responses to global warming: the Paleocene–Eocene Thermal Maximum in the eastern North Sea. *Clim. Past* **17**, 1989–2013 (2021).
84. Schoon, P. L., Heilmann-Clausen, C., Schultz, B. P., Damste, J. S. S. & Schouten, S. Warming and environmental changes in the eastern North Sea Basin during the Palaeocene–Eocene Thermal Maximum as revealed by biomarker lipids. *Org. Geochem.* **78**, 79–88 (2015).
85. Khozyem, H. et al. New geochemical constraints on the Paleocene–Eocene Thermal Maximum: Dababiya GSSP, Egypt. *Palaeogeogr. Palaeoclimatol. Palaeoecol.* **429**, 117–135 (2015).
86. Schulte, P. et al. Black shale formation during the latest Danian Event and the Paleocene–Eocene Thermal Maximum in central Egypt: two of a kind? *Palaeogeogr. Palaeoclimatol. Palaeoecol.* **371**, 9–25 (2013).
87. Frieling, J. et al. Tropical Atlantic climate and ecosystem regime shifts during the Paleocene–Eocene Thermal Maximum. *Clim. Past* **14**, 39–55 (2018).
88. Ogg, J. G., Ogg, G. & Gradstein, F. M. *A Concise Geologic Time Scale* (Elsevier, Amsterdam, 2016).
89. Frieling, J. & Sluijs, A. Towards quantitative environmental reconstructions from ancient non-analogue microfossil assemblages: Ecological preferences of Paleocene–Eocene dinoflagellates. *Earth-Sci. Rev.* **185**, 956–973 (2018).
90. Self-Trail, J. M., Powars, D. S., Watkins, D. K. & Wandless, G. A. Calcareous nannofossil assemblage changes across the Paleocene–Eocene thermal maximum: evidence from a shelf setting. *Mar. Micropaleontol.* **92–93**, 61–80 (2012).
91. Bown, P. & Pearson, P. Calcareous plankton evolution and the Paleocene/Eocene thermal maximum event: new evidence from Tanzania. *Marine Micropaleontol.* **71**, 60–70 (2009).

Acknowledgements

We thank Birgit Plessen (GFZ) for assistance with the TC, TOC, bulk organic $\delta^{13}C_{org}$ analyses and Arnold van Dijk (Utrecht University) for assistance with carbonate isotope analyses. M.Y.K., G.D.N., and A.R. acknowledge funding from European Research Council consolidator grant MAGIC 649081. The authorities in China provided the permissions for sampling.

Author contributions

M.Y.K., G.D.N. and J.F. designed the study. M.Y.K., G.D.-N., M.M. and G.Z. conducted fieldwork. M.Y.K. and J.F. performed geochemical analyses. J.F. analyzed dinocysts stratigraphy. C.F. analyzed calcareous nannofossil stratigraphy. S.Ö.A. and E.V. performed the foraminiferal biostratigraphic analyses. A.R. performed the biomarker analyses. H.T. conducted the spatial interpolation techniques. M.Y.K., G.D.-N, J.F. wrote the paper with input from all authors. All authors analyzed and discussed the data.

Competing interests

The authors declare no competing interest.

Additional information

Supplementary information The online version contains supplementary material available at https://doi.org/10.1038/s43247-022-00451-4.

Correspondence and requests for materials should be addressed to Mustafa Y. Kaya.

Peer review information *Communications Earth & Environment* thanks Sietske Batenburg and the other, anonymous, reviewer(s) for their contribution to the peer review of this work. Primary Handling Editor: Joe Aslin.

Reprints and permission information is available at http://www.nature.com/reprints

Publisher's note Springer Nature remains neutral with regard to jurisdictional claims in published maps and institutional affiliations.